metals

MDPI

Article

W-1% La_2O_3 Submitted to a Single Laser Pulse: Effect of Particles on Heat Transfer and Surface Morphology

Pasquale Gaudio, Roberto Montanari *, Ekaterina Pakhomova, Maria Richetta and Alessandra Varone

Department of Industrial Engineering, University of Rome "Tor Vergata", 00133 Rome, Italy; gaudio@ing.uniroma2.it (P.G.); pakhomovaea@mail.ru (E.P.); richetta@uniroma2.it (M.R.); alessandra.varone@uniroma2.it (A.V.)

* Correspondence: roberto.montanari@uniroma2.it; Tel.: +39-06-7259-7182

Received: 21 April 2018; Accepted: 25 May 2018; Published: 28 May 2018

Abstract: W-1% La_2O_3 has been irradiated by a single laser pulse (λ = 1064 nm, pulse duration $\tau \approx$ 15 ns, pulse energy $Ep \approx$ 4 J, spot size Φ = 200 μm, surface power density $I = 8.5 \times 10^{11}$ W·cm^{-2}) to simulate the effects of transient thermal loads of high energy occurring in a tokamak under operative conditions. The samples have been then examined by scanning electron microscope (SEM) observations to investigate erosion effects and surface morphological features. A surface depression forms in the spot central area surrounded by a ridge due to the movement of molten metal. Owing to the burst of gas bubbles, hemispherical cavities of about 10 μm and deposited droplets are observed in the ridge while the zones surrounding the ridge thermal stresses arising from fast heating and successive cooling produce an extended network of micro-cracks that often follow grain boundaries. The results are discussed and compared to those obtained in a previous work on pure bulk W.

Keywords: W-1% La_2O_3; laser; microstructure; nuclear fusion reactors

1. Introduction

Owing to its excellent thermo-mechanical properties W is a promising plasma-facing material and a candidate for building the armor which will protect the divertor of ITER (International Thermonuclear Experimental Reactor) [1–5]. W armor can be made by using tiles of bulk material or, alternatively, the parts that protect can be coated with a W layer realized through suitable deposition technologies such as plasma spray (PS) in vacuum [1,6–8], air plasma spray (APS) [9–11], physical vapor deposition (PVD) [12,13] and chemical vapor deposition (CVD) [14].

In addition to a steady state heat flux of 5–20 MW·m^{-2}, W is expected to resist transient high energy events, such as disruptions, edge localized modes (ELM) and vertical displacement events (VDE) [5]. In fact, the effects of steady thermal loads have been extensively investigated, while few papers can be found in the literature regarding transient high heat loads, which severely degrade W armor with consequent lifetime reduction, contaminate plasma and may even cause plasma disruptions [15,16].

The interaction between W and plasma has been investigated in fusion devices [17–19] or through laboratory simulations [20–30]. In previous works [29,30] a high-power laser source was used by present investigators to simulate a high thermal load released in a very short time on a small surface area (diameter ~200 μm) of PS and bulk W, and the effects of the laser pulse have been examined independent of the specific microstructural features of the samples.

Despite its remarkable characteristics such as high thermal conductivity, low vapor pressure, low tritium inventory and the highest melting point among all metals, W presents a significant drawback, namely a high ductile-to-brittle transition temperature (DBTT) that involves poor

machinability at room temperature leading to an increase of production costs. DBTT of polycrystalline W ranges from 473 to 573 K depending on specific microstructural conditions and impurity level [31]. It has been demonstrated that the addition of 1 wt. % of La_2O_3 particles dispersed into W is an effective way to overcome the problem of a scarce ductility: dispersed particles enhance toughness by strengthening grain boundaries. Moreover, with respect to pure W, W-1% La_2O_3 has higher thermal shock resistance, creep resistance and recrystallization temperature [32–34] and no grain growth was observed even after heat treatment at 1750 °C for 2 h [35].

Melt layer erosion of W-1% La_2O_3 was observed by Yuan et al. [36,37] in experiments carried out at the neutral beam facility GLADIS by applying heat loads expected for VDEs in ITER. Morphology evolution of the alloy and crack formation under transient heat loading and thermal fatigue tests were investigated by Zhang et al. [38]. Thermal fatigue tests carried out by these investigators suggested that W-1% La_2O_3 exhibits worse performance than pure tungsten when exposed to thermal loads.

The aim of the present work is to examine the specific behavior of W-1% La_2O_3 submitted to a single laser pulse in the same experimental conditions used to test PS and bulk W [30]. In particular, attention is focused on the effects of dispersed particles on heat transfer and surface morphology of the samples. The results have been discussed and compared to those obtained on bulk W.

2. Materials and Experimental

2.1. Sample Characteristics

The examined W-1% La_2O_3 was supplied by PLANSEE (Metallwerk Plansee, Reutte, Austria). The main thermo-mechanical properties are reported in Table 1.

Table 1. Thermo-mechanical properties of W-1% La_2O_3.

Properties of W-1% La_2O_3	
Density ($g \cdot cm^{-3}$)	18.90
Thermal expansion coefficient α (K^{-1})	4.7×10^{-6}
Thermal conductivity ($W \cdot cm^{-1}\ K^{-1}$)	1.20
Thermal diffusivity ($cm^2 \cdot s^{-1}$)	0.472
Young's modulus *E* (GPa)	410
Poisson's ratio	0.3
Yield Stress σ_Y (MPa)	765
Ultimate Tensile Strength (MPa)	870
Micro-hardness HV	410

After mechanical polishing the material was etched and observed by light microscopy (microscope Union Optical Co., Ltd., Tokyo, Japan). Surface etching was made by sample immersion for 90 s in a boiling solution of 1 mL H_2O_2 (30%) in 100 mL of water. The image in Figure 1 shows that the W grains have an average size of about 100 μm and La_2O_3 particles of 10–15 μm with irregular shape are homogeneously dispersed in the matrix.

Scanning electron microscopy (SEM Hitachi SU70, Hitachi, Tokyo, Japan) evidenced also La_2O_3 particles of smaller size (~1 μm). In Figure 2 the particles of larger size are indicated by yellow arrows, those of smaller size by red arrows.

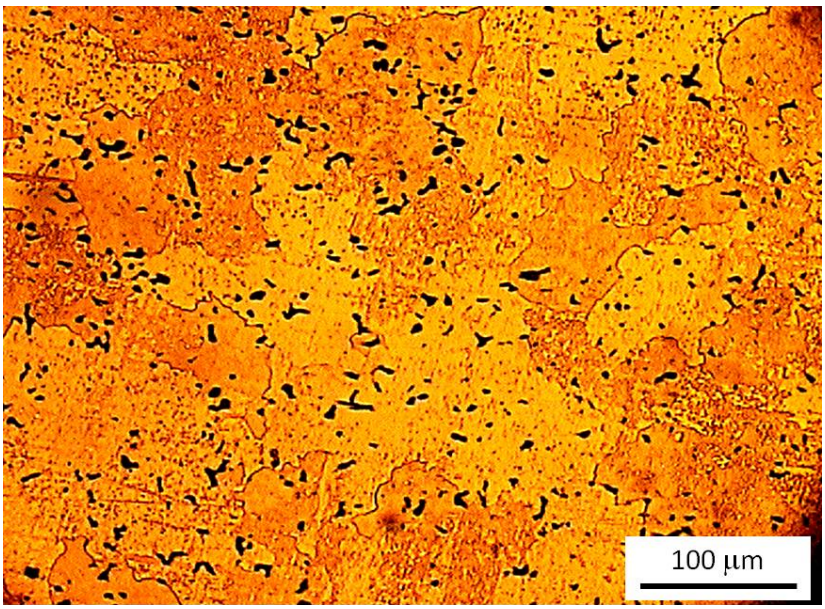

Figure 1. Light microscopy image of W-1% La_2O_3 showing the distribution of dispersed particles of larger size.

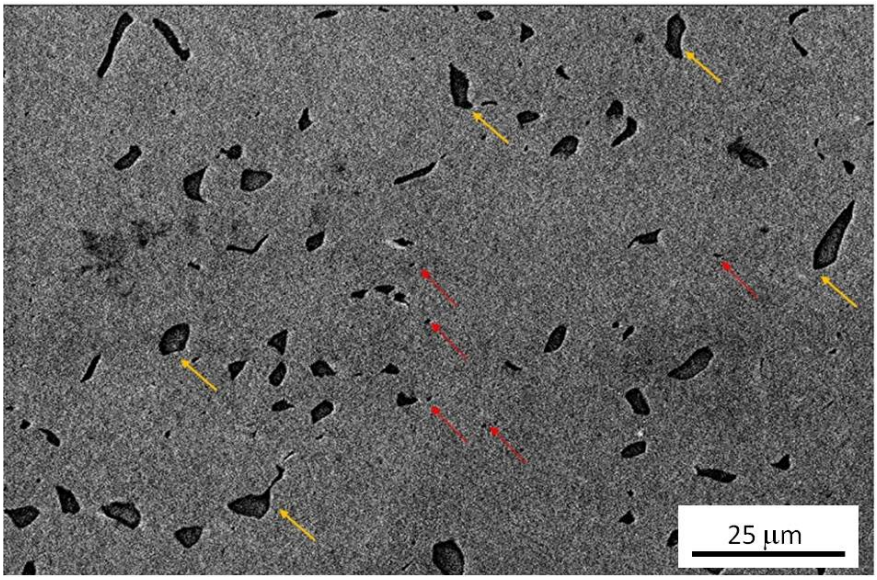

Figure 2. SEM image evidences the presence of two types of particles: the larger particles (~10–15 μm) are indicated by yellow arrows, the smaller ones (~1 μm) by red arrows.

X-ray diffraction (XRD) measurements have been carried out using a Philips PW 1729 diffractometer (Philips, Eindhoven, The Netherlands) with Cu-Kα radiation (λ = 0.15405 nm). The XRD diffractogram displayed in Figure 3 was recorded in step scanning mode with 2Θ steps of 0.05° and counting time of 5 s per step. Owing to the low amount (1 wt. %) of La_2O_3 the XRD diffractogram shows only a weak {110} reflection of the compound (file 40-1279, JCPDS-ICDD database [39]).

To investigate crystalline texture the relative intensities of the W main reflections have been compared with those of the same material with random grain orientation (file 4-806, JCPDS-ICDD database [39]). The results, summarized in Table 2, show that W grains have two weak {100} and {211} texture components.

Table 2. Comparison between the relative intensities of main reflections of W-1% La_2O_3 and those of W with random oriented grains.

{*hkl*}	Random	W-1% La_2O_3
110	100	100
200	15	27
211	23	40

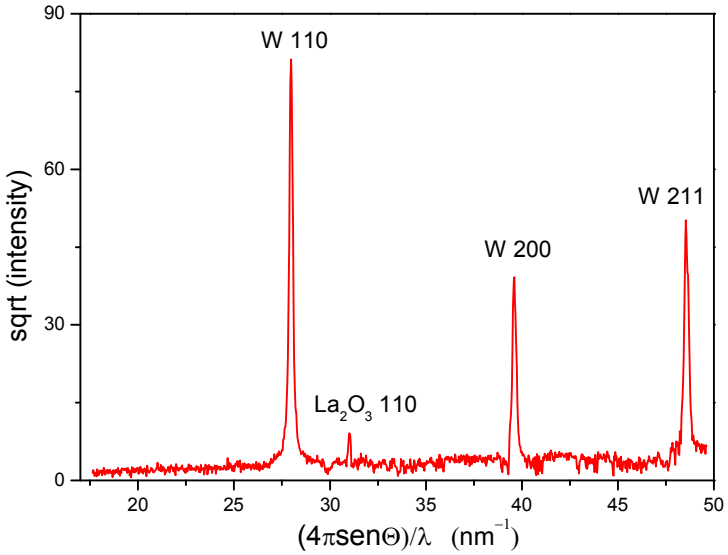

Figure 3. XRD diffractogram of W-1% La_2O_3.

2.2. Laser Source

Transient thermal loads of high energy occurring in a tokamak during operative conditions have been simulated by the interaction with a single laser pulse delivered by the Nd:YAG laser, Tor Vergata Laser-Plasma Source (TVLPS) [40]. The source used in present experiments is a non-commercial laser composed by a Nd:YAG oscillator(Quantel Sa, Orsay, France), based on Q-switched technique, followed by four amplification stages. The first two are also Nd:YAG, while the last ones are Nd:GLASS. The pulse parameters used in present experiments are: wavelength $\lambda = 1064$ nm, pulse duration $\tau \approx 15$ ns, pulse energy $Ep \approx 4$ J, Transverse Electromagnetic Mode is TEM00, P-polarized, focal spot size $\Phi = 200$ μm, surface power density on the focal plane $I = 8.5 \times 10^{11}$ W·cm^{-2}. The parameters correspond to a plasma electronic temperature $Te \approx 1.023 \times 10^6$ K at the critical surface [40] and allow simulation of the material degradation during the plasma disruption process.

To avoid spurious interaction with gases present in the atmosphere, the samples were allocated in a vacuum chamber ($P \approx 10^{-4}$ bar). Laser focusing determines levels of energy density sufficiently high to ionize elements such as O, N and C with consequent production of plasma that hinders laser-target interaction because it absorbs the major part of laser beam energy. Moreover, the specific scope of the work was to investigate the effects of plasma-W interaction in a tokamak, which operates in high vacuum conditions. A laser beam is focused on the target, mounted on a support with an incidence angle of 45° to minimize debris projection nearby target (see Figure 4).

Present experiments were carried out on polished samples; the roughness parameters $Ra = 0.024$ μm and $Rq = 0.030$ μm were measured by means of a surface roughness tester (Mitutoyo SJ-410, Mitutoyo, Kawasaki, Japan).

The total reflectivity, namely the sum of the specular reflectivity and diffuse reflectivity, has been determined for the samples in as-received condition and after mechanical polishing through a spectrophotometer (Lambda 950 from PerkinElmer Company, Waltham, MA, USA) in the wavelength

range of 400–2400 nm. For the wavelength used in these experiments (λ = 1064 nm) the reflectivity was about 60% and 48% in the case of polished and rough surface. To determine the reproducibility the same sample has been measured several times and the maximum deviation of the measured value for the total reflectivity varied by ±1.0%. In fact, the conditions are the same as those used for testing pure W and described in detail in ref. [30].

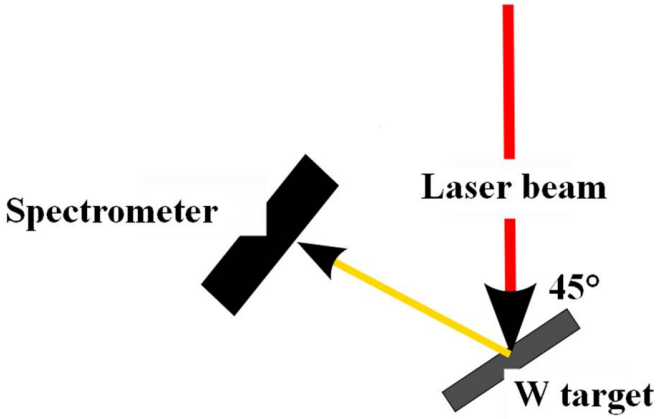

Figure 4. Experimental set-up: the laser beam is focused on the target with an incidence angle of 45°. The spectrum from plasma induced by laser pulse is recorded through a spectrometer.

The spectrum recorded from plasma induced by laser pulse was acquired in the wavelength range 300–1100 nm using a spectrometer USB 2000 model (Ocean Optics, Winter Park, FL, USA).

After laser pulse exposure the surface morphology was characterized through SEM observations and non-contact measurements carried out by means of a 3D optical profiler (New View 5000 system, Zygo Corporation, Middlefield, CT, USA).

3. Results

The laser pulse produces remarkable surface changes on an area with a diameter of about 2 mm, namely much larger than the focal spot (Φ = 200 μm). Such area can be easily identified also by visual inspection because it exhibits a brighter color with respect the other material. Figure 5 displays a SEM micrograph at low magnification of the zone affected by laser pulse.

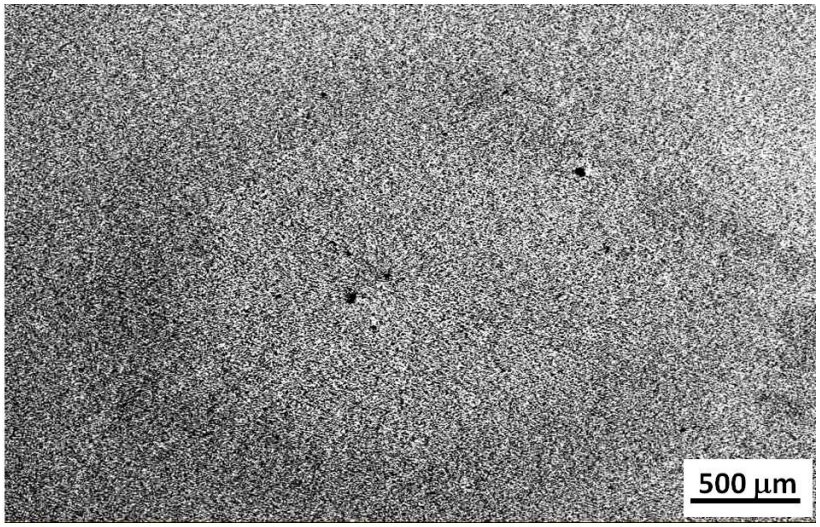

Figure 5. SEM micrograph a low magnification of the area affected by laser pulse.

In the center of the affected zone a surface depression of conical shape and diameter of about 300 µm is observed. It forms where the laser beam has the highest intensity and the major part of energy is released leading to material vaporization and melting. Since the laser pulse has a Gaussian shape a temperature gradient forms with decreasing values from the center to the periphery. Such temperature gradient determines liquid movement along the radial direction leading to the formation of a ridge around the surface depression.

In Figure 6a the zone affected by the laser pulse is that inside the red circle. The surface morphology has been carefully investigated by SEM observations performed along a radial direction from the center of the depression towards the unaffected zone. The depression (1), the ridge around it (2), the outer zone (3), the border between affected and unaffected zones (4) and the unaffected zone (5) exhibit different features depending on their specific thermal history due to the distance from the laser spot.

The depression (point 1) is shown in Figure 6b: the surface morphology with filaments oriented along the radial direction is due to the combination of two phenomena occurring in liquid metal, namely the radial movement of the molten pool and the droplet splashing, followed by re-solidification during cooling. Details at higher magnification are displayed in Figure 6c. It is noteworthy that La_2O_3 particles are not observed in the depressed zone.

On the ridge and in the zone all around the depression (points 2 and 3) there is relevant surface roughening. Thermal stresses due to fast heating and successive cooling produce an extended network of micro-cracks that often follow grain boundaries (Figure 6d,e). The compressive stresses caused by surface expansion during thermal loading and the tensile stresses caused by the shrinkage during cooling are responsible for the crack formation. Cracks often follow grain boundaries because a different crystal orientation corresponds somehow to a different heat transfer capability thus thermal stresses tend to concentrate in the boundaries. In analogous experiments the same features were already observed by us [29,30] in bulk and plasma sprayed W and by Chong et al. [23] in vacuum plasma sprayed W.

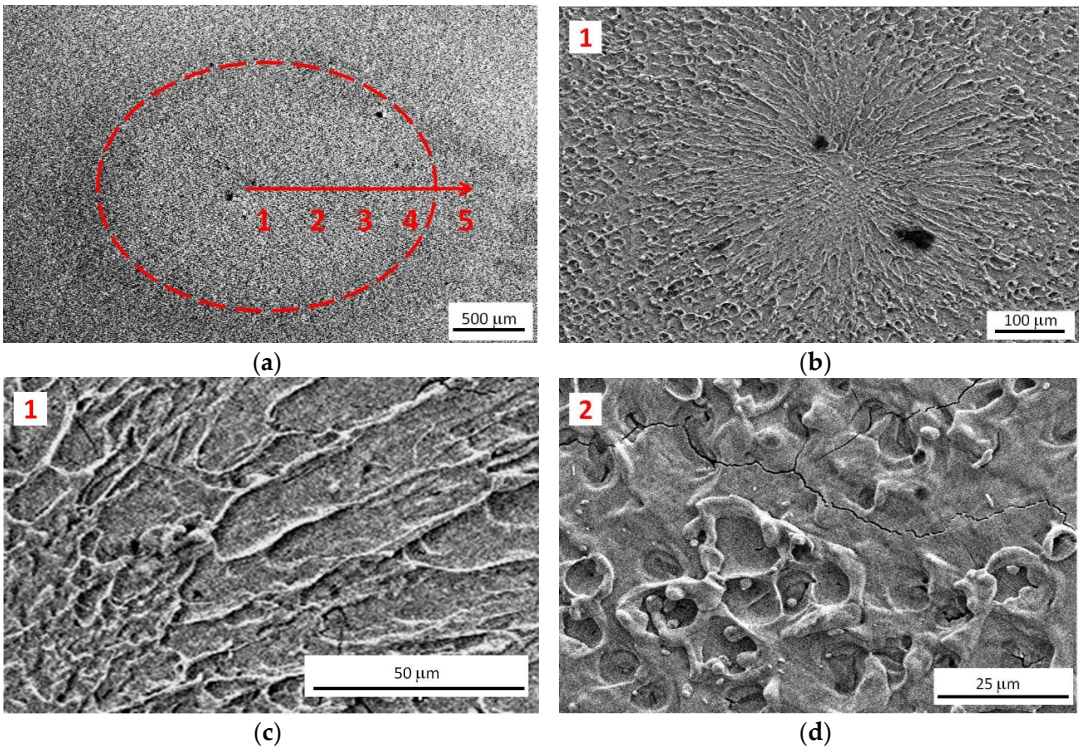

Figure 6. *Cont.*

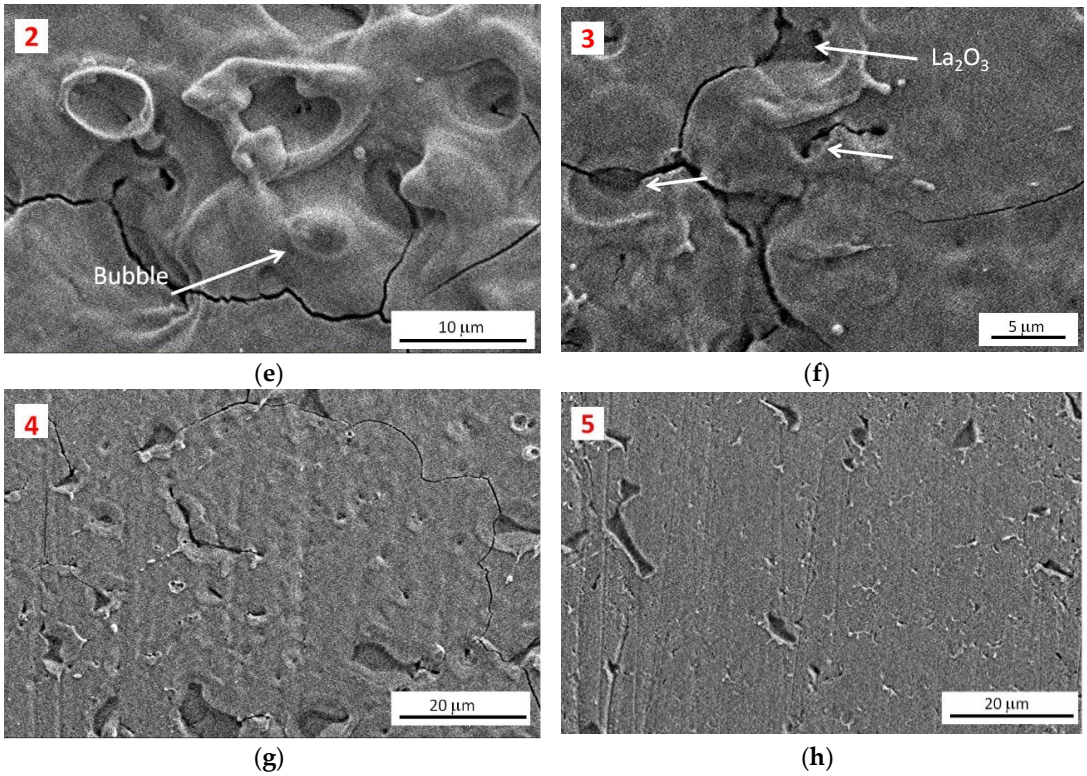

Figure 6. W-1% La_2O_3: SEM micrographs showing different zones of the area affected by laser pulse. The numbers in each micrograph correspond to the zones indicated in (**a**): the depression (**b**–**c**), the ridge around the depression (**d**–**e**), the outer zone (**f**), the border between affected and unaffected zones (**g**) and the unaffected zone (**h**).

Hemispherical cavities of about 10 µm and deposited droplets are features typical of the ridge. Such morphology, previously described by Shi et al. [41], is due to boiling in the overheated melt layer: the cavities indicate the formation and growth of bubbles that finally burst inducing droplet ejection. Some of the liquid droplets spray in the surrounding environment while others deposit on the surface of the sample. To support the aforementioned explanation about the origin of the observed cavity/droplet morphology Figure 6e displays a bubble (indicated by the arrow), which solidified before bursting.

In an outer zone (point 3) the surface is rough but hemispherical cavities are no more observed (Figure 6e); here long cracks connect the largest La_2O_3 particles (indicated by arrows). This zone underwent a thermal shock but did not melt.

The zone near the border between the affected and unaffected zones (point 4) substantially does not exhibit roughening. The surface is flat and few cracks running along grain boundaries can be observed (Figure 6g).

Finally, observations carried out in a more external position (point 5) show the typical microstructure of the as-supplied material (Figure 6h). The morphology of the area irradiated by the laser pulse, recorded by the 3D optical surface profiler, is displayed in Figure 7a.

From data collected on the irradiated area and shown in Figure 7a it was possible to determine its geometry. A representative profile is displayed in Figure 7b: the radius of the depressed region is ~150 µm, the depth ~13 µm and the ridge height ~1 µm. Profiles recorded along different directions exhibit a good repeatability; the depression depth and the ridge height are the same while slight slope changes indicate the not perfect circularity of the depression. The zone all around the ridge exhibits an irregular profile that corresponds to roughening observed by SEM.

The spectrum recorded from plasma induced by laser pulse is shown in Figure 8, where the lines of W, La and O are clearly identified. The lines of La and O are detected on visible and near infra-red parts of the spectrum. This confirms that both the phases present in the material, i.e., W and La_2O_3, underwent phase transformations leading to liquid, vapor and plasma.

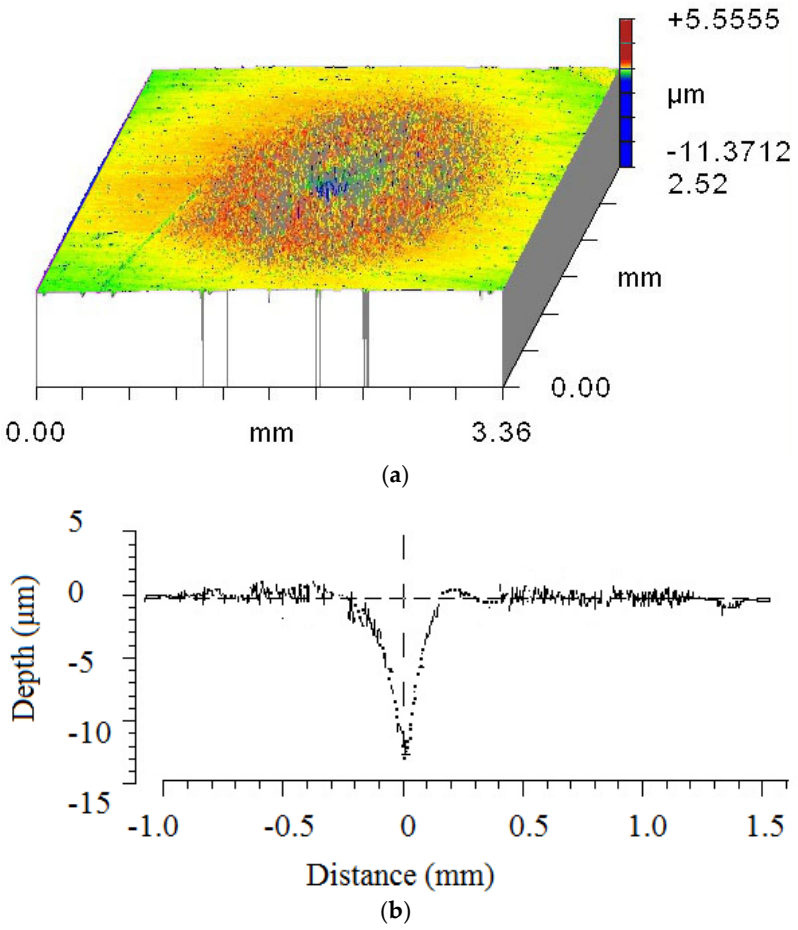

Figure 7. Morphology of the area irradiated by the laser pulse (**a**). Representative depth profile (**b**).

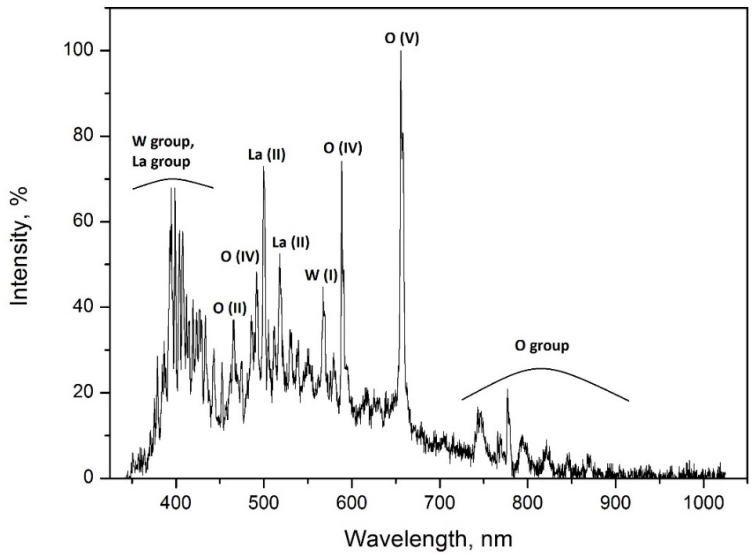

Figure 8. Spectrum recorded from plasma induced by laser pulse (wavelengths from 200 to 1100 nm).

4. Discussion

When the laser pulse hits the W-1% La_2O_3 target the electrons of the material absorb the photons from laser beam and are excited to higher energy levels in the conduction band. By the collisions of these electrons with other electrons and lattice phonons they transfer energy and increase lattice oscillations, hence the temperature of the solid. The mechanism depends on pulse duration and is described in the literature (e.g., see [42]). The conversion of light to heat occurs in a time of about 10^{-13} s, i.e., 10 orders of magnitude shorter than the laser pulse duration, thus the phenomenon can be considered as instantaneous. After the heat is generated on the material surface in correspondence of laser spot, it spreads in all directions giving rise to vaporization and melting in the zone around the spot and crack formation in the outer area. Melt layer erosion is the dominating damage mechanism for metallic armor in nuclear fusion reactors under high heat loads, and determines their lifetime. Thus, the attention of present study is focused on this point.

Owing to the rapid heating induced by the laser pulse, several physical phenomena occur in the material in successive steps and very short time.

When W matrix is still solid La_2O_3 undergoes the following phase transformations:

La_2O_3 (s) -> 2LaO (g) + 1/2 O_2 (g), enthalpy H_1 = 1.78 MJ·mol^{-1} [43], T > 2300 K;

La_2O_3 (s) -> La_2O_3 (L), enthalpy $H_2 \approx$ 0.18 MJ·mol^{-1} [44], T > 2588 K.

With reference to the solid-gas transformation the release of LaO molecules has been detected even at low power density (0.6 GW/m^2) in electron beam experiments at the Judith facility, where the surface did not show significant modification [45]. In present experiments La and O are present also in the plasma (see Figure 8).

At higher temperatures, vaporization and melting of W take place, giving rise to a pool of molten metal with gases inside. Further heating leads to melt boiling at $T \geq$ 5828 K with bubble formation.

The observed morphology of depressed area and ridge depend on: (i) heat propagation, (ii) melt motion and (iii) bubble evolution.

(i) Heat propagation

In experiments carried out on bulk W in the same conditions [30] the present authors observed the formation of an analogous morphology with conical shape, radius of ~40 μm and depth of ~75 μm. In fact, it was narrower and deeper than that observed in W-1% La_2O_3 (see Figure 9). Moreover, the erosion effect due the single laser pulse is higher in W-1% La_2O_3 than in pure W since the quantity of material removed is more than double.

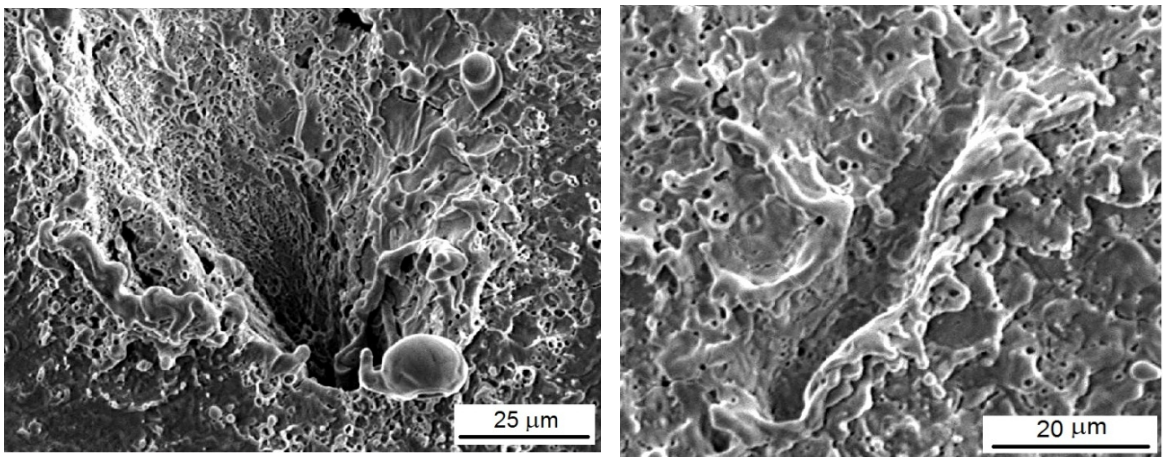

(**a**) (**b**)

Figure 9. SEM micrographs of the depression (**a**) and ridge (**b**) in bulk W [30].

This is in good agreement with the results obtained by Taniguchi et al. [46] in an electron beam irradiation facility. These investigators attributed the phenomenon to the dissociation and release from the surface of La_2O_3 particles before W melting.

To explain such differences a possible effect of crystalline texture has been considered. The speed of phonons traveling through a single crystal depends on the specific direction thus a preferred grain orientation in polycrystalline materials remarkably affects heat transfer. However, the relative intensities of the strongest XRD reflections (Table 2 in Figure 3) indicate that W-1% La_2O_3 and bulk W examined in the previous work [30] have similar textures thus such a factor cannot be considered responsible for the behavior of the two materials.

The main microstructural difference between the materials is represented by the La_2O_3 particles, which act as scattering points for phonons. In the case of pure W the scattering occurs only at grain boundaries whereas reinforcement particles in W-1% La_2O_3 are also active scattering centers. The thermal conductivity C of a polycrystalline material can be written as [47]:

$$C = \frac{C_0}{1 + \frac{C_0 R_K}{d}} \quad (1)$$

being d the mean distance between scattering centers and C_0 the grain interior thermal conductivity. C_0 depends on temperature [48]:

$$C_0 = 1.0834 - 1.052 \times 10^{-4} T + \frac{234.199}{T} \quad (2)$$

being R_K the Kapitza resistance (R_K = 2040 T^{-3} according to Khalatnikov's power law [49]), that is usually expressed in $kW^{-1} \cdot cm^2$ and represents a measure of the resistance to thermal flow [50].

Figure 10 shows the thermal conductivity of W and W-1% La_2O_3 vs. temperature, calculated through Equations (1) and (2). For bulk W the value of d is 65 μm (mean size of equiaxed grains), for W-1% La_2O_3 d = 10 μm (mean distance between La_2O_3 particles).

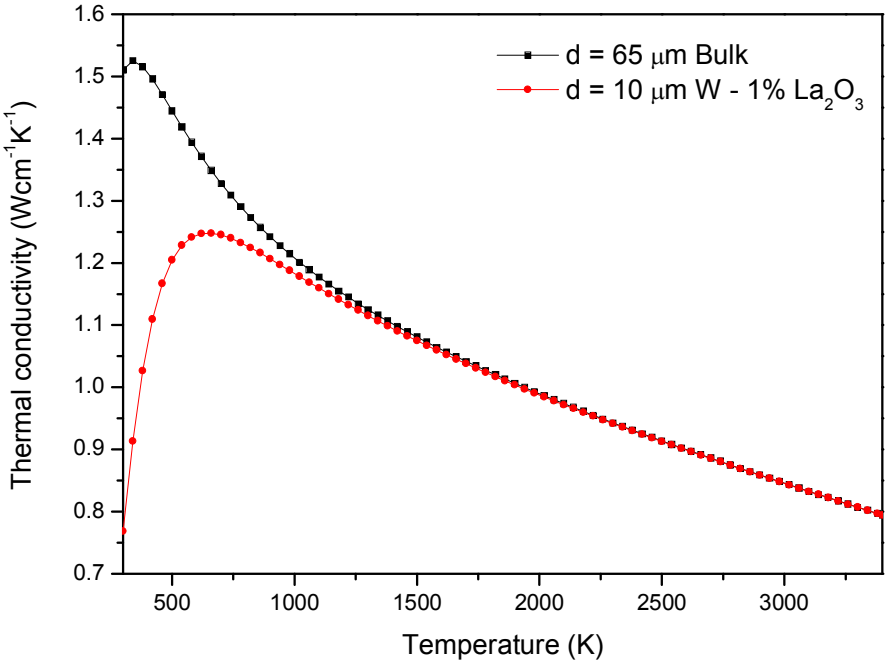

Figure 10. Thermal conductivity of W and W-1% La_2O_3 vs. temperature calculated through Equations (1) and (2).

It can be observed that above ~1250 K the effect of the mean distance of scattering centers (grain boundaries or particles) on thermal conductivity is negligible and the two curves substantially overlap whereas at lower temperatures they progressively diverge. Therefore, the heating of solid material by laser pulse is different in the two materials both in the initial stage when temperature increases and in the final stage of cooling. Owing to the larger scattering of phonons by W-1%, La_2O_3 heat tends towards a more homogeneous propagation in all the directions thus depression forms in a larger shallower area than in pure W.

(ii) Melt motion

After melting, the liquid metal is flushed to the periphery, an erosion area appears and a ridge forms around its edge. Under the assumption that the driving force for melt motion is the gradient of surface tension, Bazylev and Wuerz [51] developed a fluid dynamics simulation model to calculate the profile of depression and residual melt layer for W with different absorbed heat loads. The model considers all the forces acting on the liquid including the thermal ones. If α is the surface tension coefficient, the gradient of surface tension ($k_\alpha = \partial\alpha/\partial T$) assumes negative values. According to this model, at a given heat load the depression profile depends on k_α: the higher the gradient of surface tension, the lower the depression depth h and the ridge height h_1. Of course, as heat load increases, depression depth and ridge height increase too. Depression depth and ridge height are indicated in Figure 11, which schematically displays the depression produced by a laser pulse.

In the case of W-1% La_2O_3 the liquid metal is not made of pure W but contains also La and O coming from the molten particles. The presence of these elements in the molten pool changes the surface tension α. Although specific data are not available in the literature some basic considerations indicate that surface tension tends to increase. According to the theoretical work of Atterton and Hoar [52], confirmed by a lot of experimental evidence, the surface tension of a liquid metal is approximately proportional to the reciprocal of its atomic volume. Since the atomic volumes of W, La and O are 38.79×10^{-29} m^3, 65.45×10^{-29} m^3 and 14.71×10^{-29} m^3, respectively, the addition to W of a given amount of La and O with La_2O_3 stoichiometry leads to a melt with an average atomic volume lower than that of pure W thus α is expected to increase and a greater value involves a decrease of h and h_1 and a smoother depression-ridge morphology. Of course, greater the amount of La and O in liquid W, higher the effect. To estimate the surface tension change and consequently the quantitative agreement of present experimental results with the model of Bazylev and Wuerz [51], X-ray photoelectron spectroscopy (XPS) measurements on the depression surface are underway.

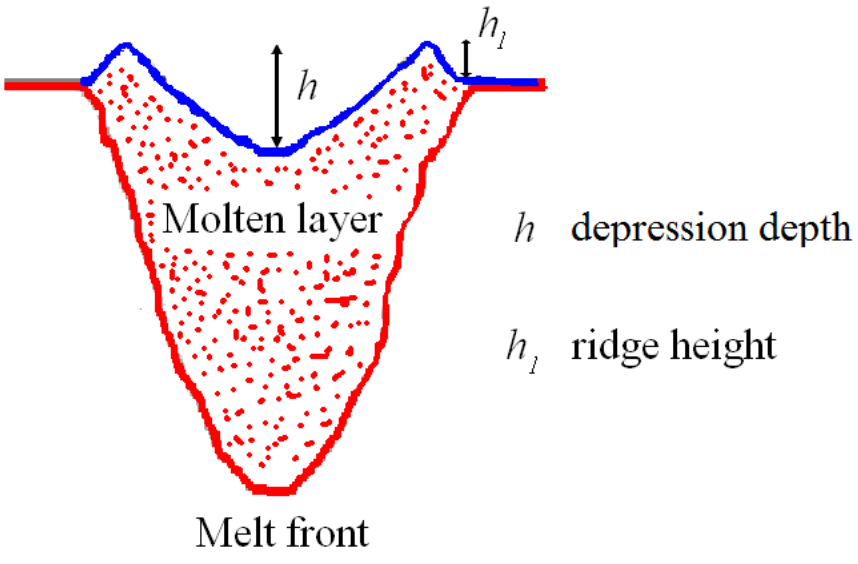

Figure 11. Schematic section of the zone affected by laser pulse.

The melt motion due to a gradient of surface tension determines the general shape of depression and ridge. The filaments oriented along the radial direction are caused by the combination of melt motion and the splashing of droplets of liquid metal due to recoil pressure effect.

(iii) Bubble evolution

The comparison of Figures 6 and 9 clearly shows that a few pores of large size (~10 μm) originated by bubble bursts are present in the ridge area of W-1% La_2O_3 while in pure W the surface of depression and ridge is scattered by a lot of small pores ($\leq$1 μm). The result, in good agreement with the findings of other investigators [53], suggests a different bubble evolution in the two materials.

Many small bubbles in pure W are clearly related to many nucleation sites, which reasonably are the impurities present in W. In the case of W-1% La_2O_3, La-gas bubbles, formed before W melting, move across the molten pool going up towards the free liquid surface driven by gravity. Along their path they swallow up the tiny impurity clusters by coalescence bringing them out of the melt. In fact, such cleaning operation strongly reduces the number of potential nucleation sites for W vapor bubbles. The result is the formation of few bubbles, which grow then to reach a larger size.

Our experiments demonstrated that W-1% La_2O_3 exhibits a worse performance than pure tungsten when exposed to laser pulses, thus pure W seems a better choice if one considers the rate of erosion and the impact on plasma of released impurities. In fact, the results support the findings of Zhang et al. [37] in thermal shock and thermal fatigue tests.

5. Conclusions

To simulate the effects of transient thermal loads of high energy occurring in a tokamak during operative conditions, the behavior of W-1% La_2O_3 submitted to single laser pulses has been investigated through SEM observations and compared to that of pure W. The results can be summarized as follows:

(i) An erosion zone forms in the laser spot central area surrounded by a ridge owing to the movement of molten metal. La_2O_3 particles are not observed in the depression because part of them is ejected while other parts melt and re-solidify together to W. In comparison to pure W the depression is larger and shallower because the particles act as scattering centers for phonons and heating is more homogeneously diffused. The morphology of depression and ridge are also affected by a different surface tension, increased by the presence of La and O atoms inside liquid W.

(ii) Hemispherical cavities of about 10 μm and deposited droplets are features typical of the ridge zone. The cavities are due to the bursting of bubbles that induces droplet ejection and subsequently deposits of some of them on the surface of the sample. Such morphology differs remarkably from that of pure W where depression and ridges are scattered with a lot of small pores ($\leq$1 μm). The explanation is given in terms of number of bubble nucleation sites for W vapor bubbles: in the case of W-1% La_2O_3 La-gas bubbles moving across the pool of liquid metal swallow up impurity clusters by coalescence and reduce the number of potential nucleation sites with the result of a few bubbles growing then to reach a larger size.

(iii) In the zone surrounding the depression ridge thermal stresses due to fast heating and successive cooling produce an extended network of micro-cracks that often follow grain boundaries. This phenomenon was observed also in pure W.

In conclusion, present experiments demonstrated that W-1% La_2O_3 exhibits a worse performance than pure W when exposed to laser pulses, thus pure W seems to be a better choice as plasma-facing material in nuclear fusion reactors if one considers the rate of erosion and the impact on plasma of released impurities.

Author Contributions: All the authors discussed and planned the experiments; M.R., P.G. performed laser tests; E.P. and A.V. prepared the samples, carried out XRD measurements and light microscopy observations; E.P. made SEM observations; all the authors contributed to analyze the results; M.R., R.M. and E.R. wrote the manuscript.

Conflicts of Interest: The authors declare no conflict of interest.

References

1. Riccardi, B.; Pizzuto, A.; Orsini, A.; Libera, S.; Visca, E.; Bertamini, L.; Casadei, F.; Severini, E.; Montanari, R.; Vesprini, R.; et al. Tungsten thick coatings for plasma facing components. *Fusion Technol.* **1998**, *1*, 223.
2. Roedig, M.; Kuehnlein, W.; Linke, J.; Merola, M.; Rigal, E.; Schedler, B.; Visca, E. Investigation of tungsten alloys as plasma facing materials for the ITER divertor. *Fusion Eng. Des.* **2002**, *61–62*, 135–140. [CrossRef]
3. Bolt, H.; Barabash, V.; Krauss, W.; Linke, J.; Neu, R.; Suzuki, S.; Nyoshida, N. Materials for the plasma-facing components of fusion reactors. *J. Nucl. Mater.* **2004**, *329–333*, 66–73. [CrossRef]
4. Lipa, M.; Durocher, A.; Tivey, R.; Huber, T.; Schedler, B.; Weigert, J. The use of copper alloy CuCrZr as a structural material for actively cooled plasma facing and in vessel components. *Fusion Eng. Des.* **2005**, *75–79*, 469–476. [CrossRef]
5. Uytdenhouwen, I.; Decreton, M.; Hirai, T.; Linke, J.; Pintsuk, G.; Van Oost, G. Influence of recrystallization on thermal shock resistance of various tungsten grades. *J. Nucl. Mater.* **2007**, *363–365*, 1099–1103. [CrossRef]
6. Montanari, R.; Riccardi, B.; Volterri, R.; Bertamini, L. Characterisation of plasma sprayed W-coatings on a CuCrZr alloy for nuclear fusion reactor applications. *Mater. Lett.* **2002**, *52*, 100–105. [CrossRef]
7. Riccardi, B.; Montanari, R.; Casadei, M.; Costanza, G.; Filacchioni, G.; Moriani, A. Optimisation and characterisation of tungsten thick coatings on copper based alloy substrates. *J. Nucl. Mater.* **2006**, *352*, 29–35. [CrossRef]
8. Kaciulis, S.; Mezzi, A.; Montanari, R.; Ucciardello, N.; Volterri, R. Composition of plasma-sprayed tungsten coatings on CuCrZr alloy. *Surf. Interface Anal.* **2010**, *42*, 1197–1200. [CrossRef]
9. Yahiro, Y.; Mitsuhara, M.; Tokunakga, K.; Yoshida, N.; Hirai, T.; Ezato, K.; Suzuki, S.; Akiba, M.; Nakashima, H. Characterization of thick plasma spray tungsten coating on ferritic/martensitic steel F82H for high heat flux armor. *J. Nucl. Mater.* **2009**, *386–388*, 784–788. [CrossRef]
10. Huang, J.; Li, X.; Chen, J.; Liu, Y.; Qi, B.; Jiang, S.; Wang, X.; Luo, G. Vacuum annealing enhances the properties of a tungsten coating deposited on copper by atmospheric plasma spray. *J. Nucl. Mater.* **2013**, *432*, 16–19.
11. Park, J.Y.; Yang, S.J.; Jin, Y.G.; Chong, R.P.; Kim, G.H.; Han, H.N. Effect of annealing with pressure on tungsten film properties fabricated by atmospheric plasma spray. *Met. Mater. Int.* **2014**, *20*, 1037–1042. [CrossRef]
12. Maier, H. Tungsten erosion in the baffle and outboard regions of the ITER-like ASDEX Upgrade divertor. *J. Nucl. Mater.* **2004**, *335*, 515–519. [CrossRef]
13. Maier, H.; Neu, R.; Greuner, H.; Hopf, C.; Matthews, G.F.; Piazza, G.; Hirai, T.; Counsell, G.; Courtois, X.; Mitteau, R.; et al. Tungsten coatings for the JET ITER-like wall project. *J. Nucl. Mater.* **2007**, *363–365*, 1246–1250. [CrossRef]
14. Hirai, T.; Kreter, A.; Linke, J.; Malzbender, J.; Ohgo, T.; Philipps, V.; Pintsuk, G.; Pospieszczyk, A.; Sakawa, Y.; Sergienko, G. Critical heat flux loading experiments on CVD-W coating in the TEXTOR tokamak. *Fusion Eng. Des.* **2006**, *81*, 175–180. [CrossRef]
15. Coenen, J.W.; Bazylev, B.; Brezinsek, S.; Philipps, V.; Hirai, T.; Kreter, A.; Linke, J.; Sergienko, G.; Pospieszczyk, A.; Tanabe, T.; et al. Tungsten melt layer motion and splashing on castellated tungsten surfaces at the tokamak TEXTOR. *J. Nucl. Mater.* **2011**, *415*, 78–82. [CrossRef]
16. Krieger, K.; Lunt, T.; Dux, R.; Janzer, A.; Kallenbach, A.; Müller, H.W.; Neu, R.; Pütterich, T.; Rohde, V. Induced tungsten melting events in the divertor of ASDEX Upgrade and their influence on plasma performance. *J. Nucl. Mater.* **2011**, *415*, 297–300. [CrossRef]
17. Tanabe, T.; Wada, M.; Ohgo, T.; Philipps, V.; Rubel, M.; Huber, A.; Von Seggern, J.; Ohya, K.; Pospieszczyk, A.; Schweer, B. Application of tungsten for plasma limiters in TEXTOR. *J. Nucl. Mater.* **2000**, *283–287*, 1128–1133. [CrossRef]
18. Krieger, K.; Maier, H.; Neu, R. Conclusions about the use of tungsten in the divertor of ASDEX Upgrade. *J. Nucl. Mater.* **1999**, *266–269*, 207–216. [CrossRef]

19. Kubkowska, M.; Skladnik-Sadowska, E.; Kwiatkowski, R.; Malinowski, K.; Kowalska-Strzeciwilk, E.; Paduch, M.; Sadowski, M.J.; Pisarczyk, T.; Chodukowski, T.; Kalinowska, Z.; et al. Investigation of interactions of intense plasma streams with tungsten and carbon fibre composite targets in the PF-1000 facility. *Phys. Scr.* **2014**, *2014*, T161. [CrossRef]
20. Merola, M.; Bobin-Vastra, I.; Cardella, A.; Febvre, M.; Giancarli, L.; Salavy, J.F.; Salito, A.; Schedler, B.; Vieider, G. Manufacturing of a full scale baffle prototype for ITER with a CFC and W plasma spray armour. *Fusion Eng. Des.* **2000**, *49–50*, 289–294. [CrossRef]
21. Zhou, Z.J.; Song, S.X.; Du, J.; Ge, C.C. High heat flux testing of tungsten plasma facing materials. *J. Nucl. Mater.* **2007**, *367–370*, 1468–1471. [CrossRef]
22. Sadowski, M.J.; Skladnik-Sadowska, E.; Malinowski, K.; Wołowskib, J.; Marchenkoc, A.K.; Tsarenkoc, A.V. Investigation of laser interaction with tungsten target by means of time-resolved optical spectroscopy. *Radiat. Effects Defects Solids* **2008**, *163*, 569–577. [CrossRef]
23. Chong, F.L.; Chen, J.L.; Li, J.G.; Zheng, X.B. Failure behaviors of vacuum plasma sprayed tungsten coatings for plasma facing application. *J. Nucl. Mater.* **2009**, *386–388*, 780–783. [CrossRef]
24. Kurehashi, H.; Ohtsuka, Y.; Ueda, Y.; Kurishita, H. Effects of repeated short heat pulses on tungsten. *J. Nucl. Mater.* **2011**, *417*, 487–490. [CrossRef]
25. Linke, J.; Loewenhoff, T.; Massaut, V.; Pintsuk, G.; Ritz, G.; Rodig, M.; Schmidt, A.; Thomser, C.; Uytdenhouwen, I.; Vasechko, V.; et al. Performance of different tungsten grades under transient thermal loads. *Nucl. Fusion* **2011**, *51*, 073017. [CrossRef]
26. Farid, N.; Harilal, S.S.; El-Atwani, O.; Ding, H.; Hassanein, A. Experimental simulation of materials degradation of plasma-facing components using lasers. *Nucl. Fusion* **2014**, *54*, 012002. [CrossRef]
27. Huber, A.; Arakcheev, A.; Sergienko, G.; Steudel, I.; Wirtz, M.; Burdakov, A.V.; Coenen, J.W.; Kreter, A.; Linke, J.; Mertens, P.; et al. Investigation of the impact of transient heat loads applied by laser irradiation on ITER-grade tungsten. *Phys. Scr.* **2014**, *T159*, 014005. [CrossRef]
28. Ouaras, K.; Colina Delacqua, L.; Quirós, C.; Lombardi, G.; Redolfi, M.; Vrel, D.; Hassouni, K.; Bonnin, X. Experimental studies of the interactions between a hydrogen plasma and a carbon or tungsten wall. *J. Phys. Conf. Ser.* **2015**, *591*, 012029. [CrossRef]
29. Richetta, M.; Gaudio, P.; Montanari, R.; Pakhomova, E.; Antonelli, L. Laser Pulse Simulation of High Energy Transient Thermal Loads on Bulk and Plasma Sprayed W for NFR. *Mater. Sci. Forum* **2017**, *879*, 1576–1581. [CrossRef]
30. Montanari, R.; Pakhomova, E.; Pizzoferrato, R.; Richetta, M.; Varone, A. Laser pulse effects on plasma sprayed and bulk tungsten. *Metals* **2017**, *7*, 454. [CrossRef]
31. Lassner, E.; Schubert, W.D. *Tungsten*; Kluwer Academic/Plenum: New York, NY, USA, 1999.
32. Kitsunai, Y.; Kurishita, H.; Kayano, H.; Hiraoka, Y.; Igarashi, T.; Takida, T. Microstructure and impact properties of ultra-fine grained tungsten alloys dispersed with TiC. *J. Nucl. Mater.* **1999**, *271–272*, 423–428. [CrossRef]
33. Leichtfried, G. Thoria-free ODS-tungsten materials. Proceeding of the Second International Conference on Tungsten and Refractory Metals, Metal Powder Industries Federation, McLean, VA, USA, 17–19 October 1994.
34. Smid, I.; Akiba, M.; Vieider, G.; Ploechl, L. Development of tungsten armor and bonding to copper for plasma-interactive components. *J. Nucl. Mater.* **1998**, *258–263*, 160–172. [CrossRef]
35. Uytdenhouwen, I.; Massaut, V.; Linke, J.; Van Oost, G. Plasma wall interaction phenomena on tungsten armour materials for fusion applications. In Proceedings of the International Youth Nuclear Congress 2008, Interlaken, Switzerland, 20–26 September 2008.
36. Yuan, Y.; Greuner, H.; Böswirth, B.; Luo, G.-N.; Fu, B.Q.; Xu, H.Y.; Liu, W. Melt layer erosion of pure and lanthanum doped tungsten under VDE-like high heat flux loads. *J. Nucl. Mater.* **2013**, *438*, S229–S232. [CrossRef]
37. Yuan, Y.; Greuner, H.; Böswirth, B.; Kriegerb, K.; Luoc, G.-N.; Xua, H.Y.; Fua, B.Q.; Lia, M.; Liua, W. Recrystallization and grain growth behavior of rolled tungsten under VDE-like short pulse high heat flux loads. *J. Nucl. Mater.* **2012**, *433*, 523–530. [CrossRef]
38. Zhang, X.; Yan, Q. Morphology evolution of La_2O_3 and crack characteristic in W–La_2O_3 alloy under transient heat loading. *J. Nucl. Mater.* **2014**, *451*, 283–291. [CrossRef]

39. *JCPDS-International Centre for Diffraction Data*. Version 2.14. 1987–1994. Available online: http://www.icdd.com/ (accessed on 27 May 2018).
40. Francucci, M.; Gaudio, P.; Martellucci, S.; Richetta, M. Spectroscopy Methods and Applications of the Tor Vergata Laser-Plasma Facility Driven by GW-Level Laser System. *Int. J. Spectrosc.* **2011**, *2011*, 792131. [CrossRef]
41. Shi, Y.; Miloshevsky, G.; Hassanein, A. Boiling induced macroscopic erosion of plasma facing components in fusion devices. *Fusion Eng. Des.* **2011**, *86*, 155–162. [CrossRef]
42. Chicbkov, B.N.; Momma, C.; Nolte, S.; Alvensleben, F.; Tünnerman, A. Femtosecond, picosecond and nanosecond laser ablation of solids. *Appl. Phys. A* **1996**, *63*, 109–115. [CrossRef]
43. Goldstein, H.W.; Walsh, P.N.; White, D. Rare earths: I. Vaporization of La_2O_3 and Nd_2O_3: Dissociation energies of gaseous LaO and NdO. *J. Phys. Chem.* **1961**, *65*, 1400–1404. [CrossRef]
44. Grundy, A.N.; Hallstedt, B.; Gauckler, L.J. Thermodynamic assessment of the lanthanum–oxygen system. *J. Phase Equilib.* **2001**, *22*, 105–113. [CrossRef]
45. Hirai, T.; Kühnlein, W.; Linke, J.; Sergienko, G. Dynamic erosion of plasma facing materials under ITER relevant thermal shock loads in the electron beam facility, JUDITH. In Proceedings of the 20th IAEA Fusion Energy Conference, Vilamoura, Portugal, 1–6 November 2004; IAEA Publications: Brussels, Belgium, 2004; pp. 111–2004.
46. Taniguchi, M.; Nakamura, K.; Sato, K.; Ezato, K.; Yokoyama, K.; Akiba, M. Disruption Erosion Tests on La_2O_3 Containing Tungsten Material. *Fusion Technol.* **2001**, *39*, 890–893.
47. Swartz, E.T.; Pohl, R.O. Thermal boundary resistance. *Rev. Mod. Phys.* **1989**, *61*, 605–668. [CrossRef]
48. Nan, C.-W.; Birringer, R.; Clarke, D.R.; Gleiter, H. Effective thermal conductivity of particulate composites with interfacial thermal resistance. *J. Appl. Phys.* **1997**, *81*, 6692–6699. [CrossRef]
49. Ho, C.Y.; Powell, R.W.; Liley, P.E. *Thermal Conductivity of the Elements: A Comprehensive Review*; American Institute of Physics: New York, NY, USA, 1974; pp. 1–796.
50. Johnson, R.C.; Little, W.A. Experiments on the Kapitza resistance. *Phys. Rev.* **1963**, *130*, 596–604. [CrossRef]
51. Bazylev, B.; Wuerz, H. Melt layer erosion of metallic armour targets during off-normal events in tokamaks. *J. Nucl. Mater.* **2002**, *307–311*, 69–73. [CrossRef]
52. Atterton, D.V.; Hoar, T.P. Surface tension of liquid metals. *Nature* **1951**, *167*, 602. [CrossRef] [PubMed]
53. Yuan, Y.; Xu, B.; Fu, B.Q.; Greuner, H.; Boswirth, B.; Xu, H.Y.; Li, C.; Jia, Y.Z.; Qu, S.L.; Luo, G.-N.; et al. Suppression of cavitation in melted tungsten by doping with lanthanum oxide. *Nucl. Fusion* **2014**, *54*, 1–9. [CrossRef]